

# UV-VIS laser parameter effects on the physicochemical properties of Laser-Induced Graphene

Jhonattan de la Roche<sup>1,2\*</sup>, Carlos Lubo-Mestanza<sup>1,2</sup>, Laura Tenjo-Patiño<sup>1,2</sup>, Santiago Lasso<sup>2</sup>,  
Santiago Ospina-Arroyave<sup>2</sup>, Sebastián Mendoza<sup>2</sup>, Lucero Alvarez-Mino<sup>1</sup>

## Edited by

Angela Johana Espejo Mojica  
editorus@javeriana.edu.co

1. Universidad Nacional de Colombia, Facultad de Ciencias Exactas y Naturales, Departamento de Física y Química, campus La Nubia km 9 vía al aeropuerto, Manizales, Colombia.  
. Materials Science Laboratory - MLS, Caldas Technology Industries SAS, campus La Nubia km 9 vía al aeropuerto, Manizales, Colombia.

\*jdey@unal.edu.co.

Received: 17-04-2024

Accepted: 28-03-2025

Published online: 07-06-2025

**Citation:** de la Roche J, Lubo-Mestanza C, Tenjo-Patiño L, Lasso S, Ospina-Arroyave S, Mendoza S, Alvarez-Mino L. UV-VIS laser parameter effects on the physicochemical properties of Laser-Induced Graphene, *Universitas Scientiarum*, 30: 107-126, 2025  
doi: 10.11144/Javeriana.SC30.ulpe

**Funding:** n.a.

**Electronic supplementary material:** supp. 1



## Abstract

Laser-induced graphene (LIG) is a versatile and scalable technique for the low-cost production of graphene-like sensing devices. However, the performance of these devices is hypersensitive to the engraving parameters used during fabrication. In this work, we systematically varied laser engraving speed and power to explore their influence on the physical and electrochemical properties of LIG electrodes to achieve low resistance, high LIG porosity, and enhanced sensitivity for future sensing applications. We employed a UV-VIS diode laser mounted on a CNC (Computer Numerical Control) system constructed by our team to engrave on polyimide sheets. Our results demonstrated that low and high-power settings led to poor electrode performance due to increased resistivity and structural damage. Conversely, electrodes fabricated at power settings between 60 % (3W) and 80 % (4W) of the laser's maximum capacity, combined with maximum operable speed, exhibited uniform morphology, high conductivity, and reversible electrochemical behavior. Under these conditions, the resulting LIG-based electrodes featured porous graphene on networks with directional asymmetry, with an  $I_D/I_G$  ratio of approximately 1.3, a sheet resistance of 20  $\Omega$ /sq, and a peak current of 272.1  $\mu$ A, alongside an  $I_{pa}/I_{pc}$  ratio near 1 in cyclic voltammetry measurements, providing a foundation for the development of efficient LIG-based sensors.

**Keywords:** Laser-induced graphene (LIG); engraving parameters; UV-VIS diode laser; electrochemical properties; microstructure.

## 1. Introduction

Graphene is a two-dimensional carbon allotrope composed of a single layer of atoms arranged in a hexagonal lattice, which exhibits properties such as high electrical and thermal conductivity, optical transparency, high electron mobility at room temperature, fast electron transfer rate, large surface area, and outstanding mechanical strength [1–6]. Due to these properties, graphene has gained attention in various applications, particularly in sensor technology, flexible electronics, environmental care, energy storage and generation, and medicine [2, 3, 7–13].

One promising and cost-effective method for synthesizing graphene is Laser-Induced Graphene (LIG), introduced in 2014 as a technique capable of converting carbon-based materials into porous graphene using conventional CO<sub>2</sub> laser cutters [14]. This method does not require chemical reagents, cleanroom environments, or expensive equipment, making it an accessible alternative to produce graphene [6, 12, 15–19]. Since its introduction, various studies have explored LIG use with different laser types across the UV-visible and infrared spectrums applied on substrates

such as polyimide (PI) and other polymers [8–10, 14, 20, 21]. These studies consistently highlight the influence of laser parameters—such as speed, power, and wavelength—on the quality of the produced LIG and its resulting properties, particularly in electrical conductivity and morphology.

Polyimide (PI) remains the most commonly used substrate for LIG synthesis due to its capacity to form porous graphene through laser-induced thermal and photochemical processes, breaking C-N, C-O, and C=O bonds [22]. Previous research revealed that as power and fluence increase, PI turns into LIG of different morphologies, such as isotropic pores, anisotropic networks, or nanofibers, depending on the fluence applied [23], [24]. While CO<sub>2</sub> lasers remain the leading tools, UV-VIS diode lasers are emerging as a more precise and affordable option, offering higher resolution and more efficient bond-breaking capabilities [11, 25, 26].

For sensor applications, it is essential to produce LIG with low sheet resistance and a porous structure, as these characteristics improve electron transfer rates and surface area, both of which are key for detecting biomolecules at low concentrations. High conductivity ensures that the changes in current caused by interactions between the graphene and biomolecules are accurately detected, making it a crucial parameter for optimizing sensor performance [27], [28].

In this work, we varied the power and speed, as engraving parameters, to produce LIG electrodes for future sensing applications using a UV-VIS diode laser mounted on a CNC system constructed by our team. We analyzed the effect of these parameters using various characterization techniques, including optical microscopy, scanning electron microscopy (SEM), Raman spectroscopy, and cyclic voltammetry, which provided insights into electrode morphology, structural defects, and electrochemical performance. This approach contributes to understanding LIG fabrication parameters and their impact on sensor performance. Moreover, our work fosters local technological development by enabling the adaptation of nano-fabrication techniques through the synchronized integration of components, resulting in a complete system capable of synthesizing nanomaterials at a lower cost than traditional graphene production methods.

## 2. Materials and methods

### 2.1. LIG-based electrode fabrication

LIG-based electrodes were fabricated using a 5 W transistor-transistor-logic (TTL) laser ( $\lambda = 450$  nm) mounted on a custom-built CNC (Computer Numerical Control) system. This system, controlled by the Laser GRBL (v5.4.0) software, enabled precise tool movement to fabricate intricate electrode designs. The electrode design was developed using Autodesk Inventor Professional (v2021) and exported in portable network graphics (.png) format at a resolution of 913×1041 pixels. A 3-electrode configuration was used, incorporating a working electrode (WE) with a diameter of 3.5 mm and a total area of 30.5 mm<sup>2</sup>, a counter electrode (CE) with a total area of 32 mm<sup>2</sup>, and a reference electrode (RE) with a total area of 28.2 mm<sup>2</sup>. The design choices were based on commercially available models and insights from relevant literature. These dimensions were selected to ensure compatibility with our potentiostat for conducting precise electrochemical measurements. Laser power and speed settings were adjusted for engraving different samples within 10 % to 100 % and 30 % to 91 % of the system's maximum operational capacity, respectively. These percentages represent relative adjustments based on the machine's capabilities, with 100 % corresponding to the highest achievable power (5 W) and speed (1750 mm/min) for this specific setup.

The engraving was performed on polyimide (PI) sheets (125  $\mu\text{m}$  thick) sourced from Shijiazhuang Dadao Packaging Materials Co. LTD. The sheets were first thermally treated at 200 °C for 20 minutes, using a Challenger hot air oven (model HAF 2023) to relieve mechanical stress. A vinyl layer was then adhered to the surface to improve resistance to heat deformation, thickness, and stiffness during the laser engraving process. Silver (Ag) ink was applied to the terminals of the three electrodes. This protective layer prevents damage to the LIG during repeated insertion and potentiostat connection removal, which is connected to a computer for real-time measurements. Silver/Silver Chloride (Ag/AgCl) ink was applied to the top of the reference electrode to establish a reference for cyclic voltammetry in electrochemical experiments. After application, electrodes were dried in an oven at 75°C for 40 minutes to ensure proper adhesion and stability of the ink layers. A microfluidic tape was applied to cover the body of the three electrodes to facilitate handling and prevent contamination during electrochemical measurements.

## 2.2. Characterization

The sheet resistance of different samples was determined by measuring the electrical resistance ( $R$ ) at the extreme points across the length of rectangular electrodes with the WE dimensions, using a UNI-T UT61E+ digital multimeter. Next, the sheet resistance ( $R_s$ ) formula was applied:

$$R_s = R \times \frac{W}{L} \quad (1)$$

where  $W$  and  $L$  are the electrode width and length, respectively. This process was repeated for three samples engraved with the same parameters, and the average resistance value was calculated.

The working electrode sample was subjected to morphological characterization, and the circular working electrode area was carefully isolated for optical microscopy and SEM imaging. These sections were then mounted onto the SEM sample holder using conductive carbon tape. Morphology was examined using a digital LED microscope (Elikliv EDM 9), followed by high magnification imaging conducted using a Thermo Fisher Helios 5 Dual Beam scanning electron microscope (SEM) at low acceleration voltage (< 5kV). Structural characterization by spectroscopy was performed on LIG 20-100 samples, with each sample analyzed in triplicate, using a Thermo Fisher DXR SmartRaman spectrometer equipped with a 532 nm laser and a power of 6 mW, covering a range of 1000  $\text{cm}^{-1}$  to 3000  $\text{cm}^{-1}$ . The results were averaged, and their standard deviations were calculated.

Electrochemical characterization was performed via cyclic voltammetry using the PSTrace 5.9 software. The measurements were taken in a solution of 2 mM potassium ferricyanide ( $\text{K}_3[\text{Fe}(\text{CN})_6]$ ), 2 mM potassium ferrocyanide ( $\text{K}_4[\text{Fe}(\text{CN})_6]$ ), and 0.1 M potassium chloride (KCl), using a PalmSens EmStatPico module. The potential range spanned 0.35 V to 0.70 V with scan rates of 0.02 V/s, 0.05 V/s, 0.1 V/s, 0.15 V/s, and 0.2 V/s, and a step size of 0.01 V. The effective surface area of the electrodes was determined using the Randles-Sevcik equation at 25 °C. **Fig. 1** illustrates the overall described process for fabricating LIG-based electrodes.

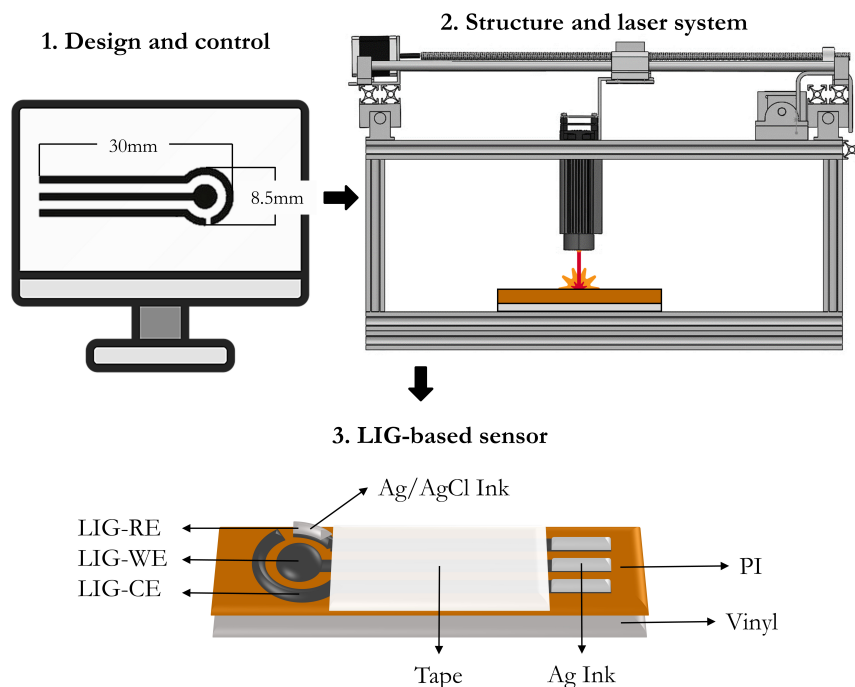


**Figure 1.** Diagram of the step-by-step process for fabricating LIG-based electrodes. (1) Electrode design and control are managed using Autodesk software and Laser GRBL for engraving. (2) A custom-built CNC system integrates a diode laser to engrave polyimide sheets, forming the electrode patterns. (3) The final LIG electrodes, with Ag ink applied to contact terminals and Ag/AgCl on the reference electrode, are prepared for testing.

### 3. Results and discussion

As explained earlier, low sheet resistance is crucial for achieving high biosensor sensitivity, which is our primary goal. We explored various samples produced under different speed and power settings to identify the conditions that yield the best conductivity results. For this purpose, we conducted a preliminary characterization of the equipment, where the focus and lines per millimeter (quality) were fixed at 5 mm and 20 lines/mm, respectively. Additionally, the experimental speed of the engraving process was determined and compared with the theoretical speed set in the software. We observed that the maximum velocity could only be achieved up to approximately 91 % of the theoretical speed, as higher settings introduced mechanical vibrations that caused inconsistencies in the engraving process. Further details on these tests are provided in Supplemental Fig. 1.

We generated a sheet resistance map by varying the engraving speed and power during electrode fabrication. **Fig. 2a** shows the colormap of the sheet resistance for the working electrodes (WE) as a function of speed and power. Three distinct zones emerge according to the sheet resistance values range: the light green zone (0-35  $\Omega/\text{sq}$ ), the dark green zone (35-70  $\Omega/\text{sq}$ ), and the white zone, where the electrodes exhibit no conductivity or have a resistance higher than 70  $\Omega/\text{sq}$ . As previously mentioned, 91 % (1592.5 mm/min) represents the maximum operational speed, so the speed range is limited to this value.

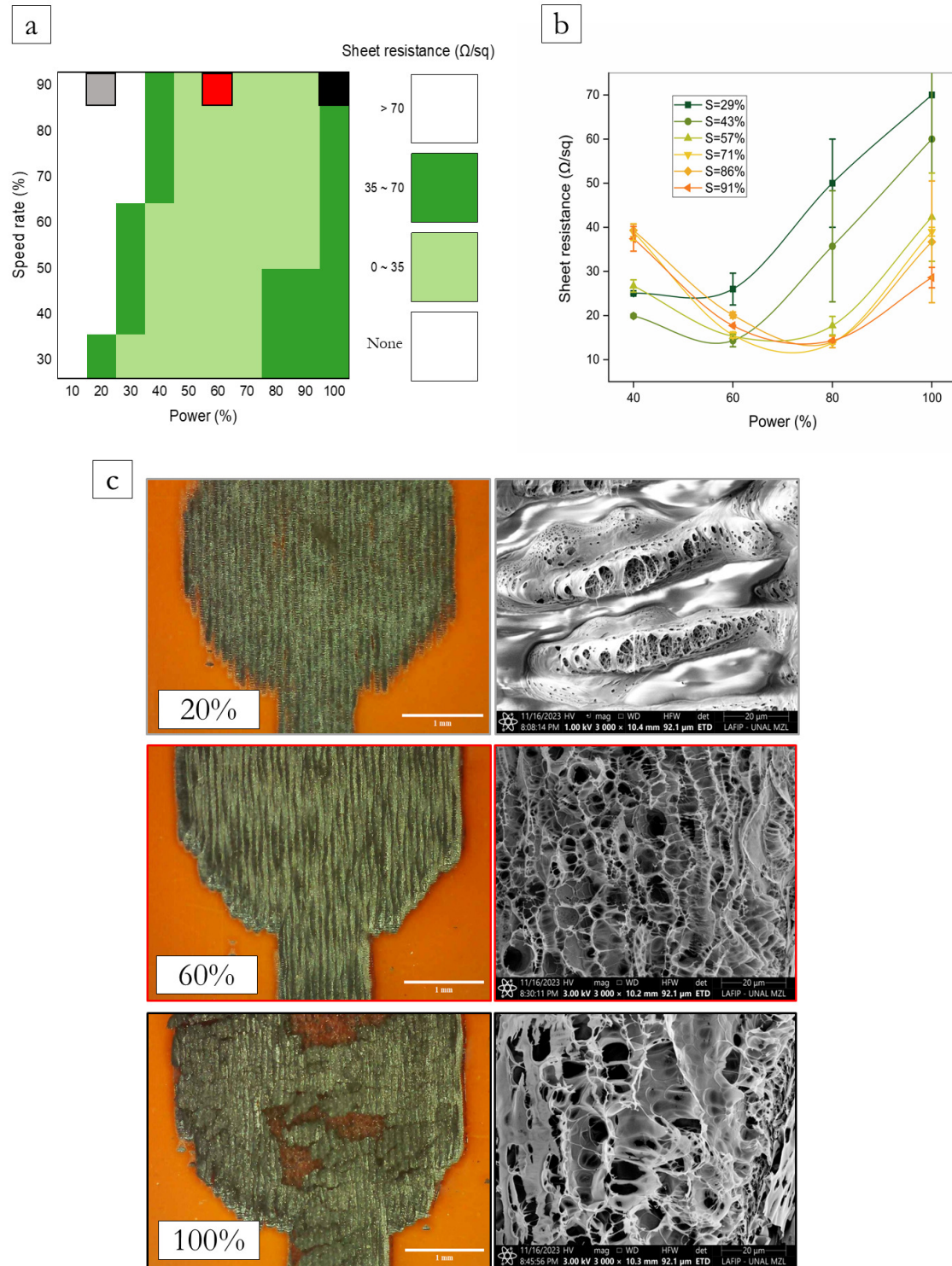


**Figure 2.** Electric and morphological properties of LIG (a) sheet resistance colormap varying power and speed rate. (b) Sheet resistance vs power for different speed values. (c) Optical and SEM images showing the different morphologies of LIG.

Fig. 2b shows the relationship between sheet resistance (Y-axis) against power (X-axis) for six different speed rates ( $S$ ), excluding the white zone of Fig. 2a, where no conductivity was observed. The plotted speed rates are 29 % (507.5 mm/min), 43 % (752.5 mm/min), 57 % (997.5 mm/min), 71 % (1242.5 mm/min), 86 % (1505 mm/min), and 91 % (1592.5 mm/min). The features of the three representative zones in Fig. 2a (grey, red, and black squares) were further explored via optical and scanning electron microscopy imaging at 91 % speed, with 20 % (1 W), 60 % (3 W), and 100 % (5 W) power values (LIG20, LIG60, and LIG100, respectively), and are shown in Fig. 2c. Although we had the flexibility to choose any other speed, which also provides us with the desired zones of interest, we chose the maximum speed at which the CNC structure functions optimally, balancing productivity and time efficiency, aligning with one of the key advantages of LIG, which is the potential for rapid and large-scale production. These regions were chosen because their properties change notably with different power settings and correspond to three colored squares in Fig. 2a at 91 % speed and power settings of 20 % (gray square), 60 % (red square), and 100 % (black square).

As seen in Fig. 2a, the best conductivity results were achieved when the power was within its mid-range values (light green zone). Our best value obtained was  $13.3 \Omega/\text{sq}$ , which is comparable with excellent values of sheet resistance for UV-VIS lasers [29–32] and for infrared ( $\text{CO}_2$ ) lasers [14, 33–37] reported in the literature. The specific starting power value for this light green zone depended on the engraving speed, as the zone shifted diagonally toward higher speeds. At lower speeds, the laser power is applied for a longer duration over the same area, resulting in overheating and an accelerated transformation of the polyimide, leading to better conductivity and allowing it to swiftly reach the threshold of the dark green zone in Fig. 2a. This behavior was also illustrated by the trends observed in the curves for each speed in Fig. 2b. For instance, at lower speeds, the shapes of the curves appear less balanced along the power axis. In these cases, the initial part of the curve (below mid-low power values) exhibits significantly lower resistance than the final part (high power values). This results in a tilted appearance where the vertex does not center along the horizontal axis. We categorize power as follows: 0–20 % (Low, 0–1 W), 20 % – 40 % (Mid-low, 1–2 W), 40 % – 60 % (Mid-range, 2–3 W), 60 % – 80 % (Mid-high, 3–4 W), and 80 % – 100 % (High, 4–5 W).

In contrast, as the speed increased, the white region in Fig. 2a expanded, delaying entry into the dark green zone. In Fig. 2b, the curves at higher speeds show a more balanced resistance distribution, with values that are more similar at both low and high-power settings. This results in a more centered vertex, indicating a uniform power response on resistance. This effect contributes to a more even distribution of resistance across power values, which provides a broader range with lower resistivity (light green zone) and aligns with the earlier discussed power-time effect, where at high speeds, the laser takes a longer time to sufficiently engrave and initiate the transformation of the polyimide into porous structures, followed by its conversion into LIG. Additionally, at higher speeds, fewer error margins for sheet resistance occurred than at other speeds, ensuring better repeatability in the results (Fig. 2b).

In Fig. 2c, we observe three optical micrographs that support these findings, revealing regions with higher electrical resistance (at 20 % and 100 % power) due to surface non-uniformity. However, it is now clear that the underlying causes differ between these two regions. At low power, visible holes contribute to the higher resistance, as lines did not overlap sufficiently to create a uniform conduction area. At high power, excessive line overlap led to burnt areas and morphological damage, as seen in the LIG100 electrodes, disrupting surface connectivity and increasing electrical resistance. In contrast, the 60 % power zone exhibits the most uniform surface, which correlates with better conductivity.

The LIG20 SEM image in Fig. 2c revealed disconnected LIG pores, explaining the lack of electrical conduction and increased resistance. We identified this stage (around 20 % power) as the carbonization phase described by Abdulhafez *et al.* [23]. At 40 % power, the morphology shows how LIG pores begin to interconnect, indicating a progression in the carbonization phase (see Supplemental Fig. 2). At LIG60, we identified an LIG with a balanced proportion of low and high fibers, suggesting the onset of anisotropic cellular network [23] and indicating an interconnected structure that enhances conductivity. These LIG-fibers, described by Duy *et al.* in 2018 [24], can facilitate charge transport, as denser networks of interconnected graphene tend to reduce electron scattering. As power increased to 80 % (Supplementary information Fig. S2), we observed even more prominent LIG-fibers (LIGF) than for LIG60, consistent with the LIG to LIG-fibers transition (formation of loosely interconnected fibrous structures) [24]. Finally, LIG100 revealed larger pores than the previous powers, with an evident wooly fiber morphology [23].

Thus, the least resistance was achieved within a 50 % to 70 % power range regardless of speed (light green zone), producing LIG-based working electrodes with excellent electrical properties. Resistance is higher at low- and high-power values but lower at intermediate-power values, reaffirming the importance of tuning the energy strength applied, so that the right amount achieves the desired degree of carbonization and sheet resistance.

**Fig. 3a** shows the Raman spectrum for LIG20, LIG40, LIG60, LIG80, and LIG100, all fabricated at a 91 % speed rate to maintain consistency with the engraving settings of electrodes analyzed in Fig. 2c. The insets provide a zoomed-in view of the graph, focusing on the observed D, G and 2D peaks. Fig. 3b shows the graph of these intensity peak ratios ( $I_D/I_G$  and  $I_{2D}/I_G$ ) as a function of power.

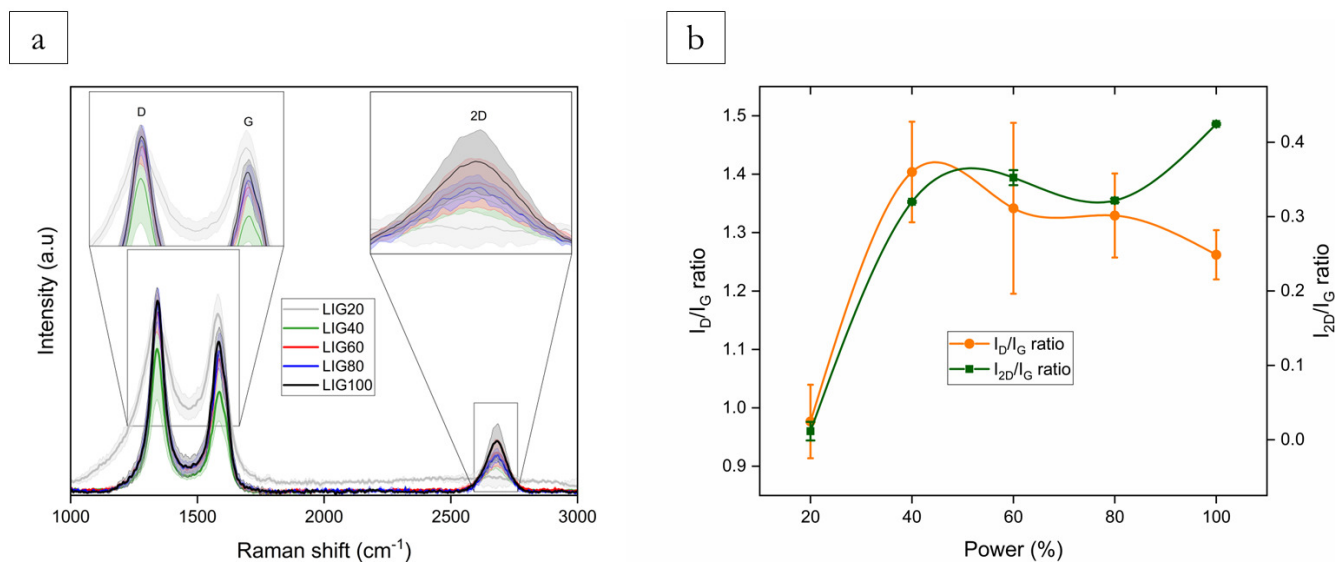


**Figure 3.** (a) Raman spectrum as a function of power. The shaded area around the lines shows the deviation. (b) Graph of  $I_D/I_G$  and  $I_{2D}/I_G$  ratios as a function of power.

The Raman spectrum in Fig. 3a revealed characteristic graphene bands, as follows: the D band at  $\sim 1350\text{ cm}^{-1}$ , the G band at  $\sim 1,580\text{ cm}^{-1}$ , and the 2D band at  $\sim 2700\text{ cm}^{-1}$  [38]. In Fig. 3b, for intermediate power values, the  $I_D/I_G$  ratio (the intensity of the D band compared to the intensity of the G band) is  $\sim 1.3$ , indicating a high number of defects in the graphene structure. The D band is associated with defect-induced scattering processes, meaning that as the number of defects increases, the intensity of the D band rises relative to the G band. This suggests that the material has undergone some level of disorder. In contrast, the  $I_{2D}/I_G$  is  $\sim 0.35$ . Since the 2D band indicates the quantity and order of graphene layers present in the material, this suggests a porous multilayered structure, as values above 2 typically signify a single-layer structure [24, 35, 39]. The D peak remained constant across all power values. However, the  $I_D/I_G$  ratio decreased as the power of engraved electrodes increased. Conversely, the  $I_{2D}/I_G$  ratio increased as a function of power comparing LIG20 and LIG100 while remaining constant for intermediate power values. These trends suggest that higher power facilitates the transformation to porous graphene and improves its structural integrity, thereby reducing defects and enhancing the quality and quantity of graphene layers. These findings indicate a direct correlation between the alterations in the Raman peaks and the structural changes in LIG under varying laser energy levels, as power settings influenced the balance between defect introduction and graphene layer growth. This is consistent with the observations of Herziger *et al.* [40], who noted that the  $I_D/I_G$  ratio increases progressively up to a peak value before starting to decrease. We observed this peak at 40 % power, after which  $I_D/I_G$  ratio declined.

We recorded cyclic voltammograms (CV) for different scan rate values at 91 % speed, the same speed used for the Raman, optical, and SEM analyses to consistently characterize the fabricated electrodes and systematically explore the electrochemical responses of the selected zones in Fig 2c. Figs. 4a-4c depict the CV curves for LIG20, LIG60, and LIG100. To find each electrode's effective area, a corroboration of its dependence on diffusion was first tested by plotting the relationship between peak currents and the square root of the scan rate. Fig. 4d presents the calibration curves for five different scan rates applied to the tested electrodes (LIG40, LIG60, LIG80, and LIG100). Whereas Fig. 4e depicts their effective area as a function of power.

Electrodes subjected to 20 % power were evaluated only at a scan rate of 0.1 V/s. Yet, they failed to exhibit any discernible electrochemical response as the voltammogram lacks the expected characteristic form for a ferri-ferrocyanide redox reaction without observable peak currents. Following the Randles-Sevcik equation, which states a direct proportionality between scan rate ( $v$ ) and peak current ( $I_p$ ), the highest scan rate (0.2 V/s) yielded the highest peak current across the remaining electrodes (for LIG40 and LIG80, see Supplemental Fig. 3). The remaining tested electrodes' voltammograms revealed their reversibility and sensitivity. An  $I_{pa}/I_{pc}$  ratio close to 1 indicates a reversible process ( $I_{pa}$  is the anodic peak current measured at the oxidation peak, and  $I_{pc}$  is the cathodic peak current measured at the reduction peak). The peak current is proportional to analyte concentration according to the Randles-Sevcik equation, and a higher value suggests that the electrode generates a stronger response to a given analyte concentration, indicating greater sensitivity. LIG40 exhibited the most significant differences in the anodic and cathodic peak currents among all tested electrodes. Consequently, its  $I_{pa}/I_{pc}$  ratio deviated the furthest from 1, indicating a reversibility below that of the other electrodes. Conversely, LIG60 presented an  $I_{pa}/I_{pc}$  relation closer to 1, while LIG80 exhibited almost identical  $I_{pa}$  and  $I_{pc}$  currents. This symmetry indicates a reversible electrochemical process as the engraving power increases, highlighting the electrode's ability to undergo efficient oxidation and reduction reactions.

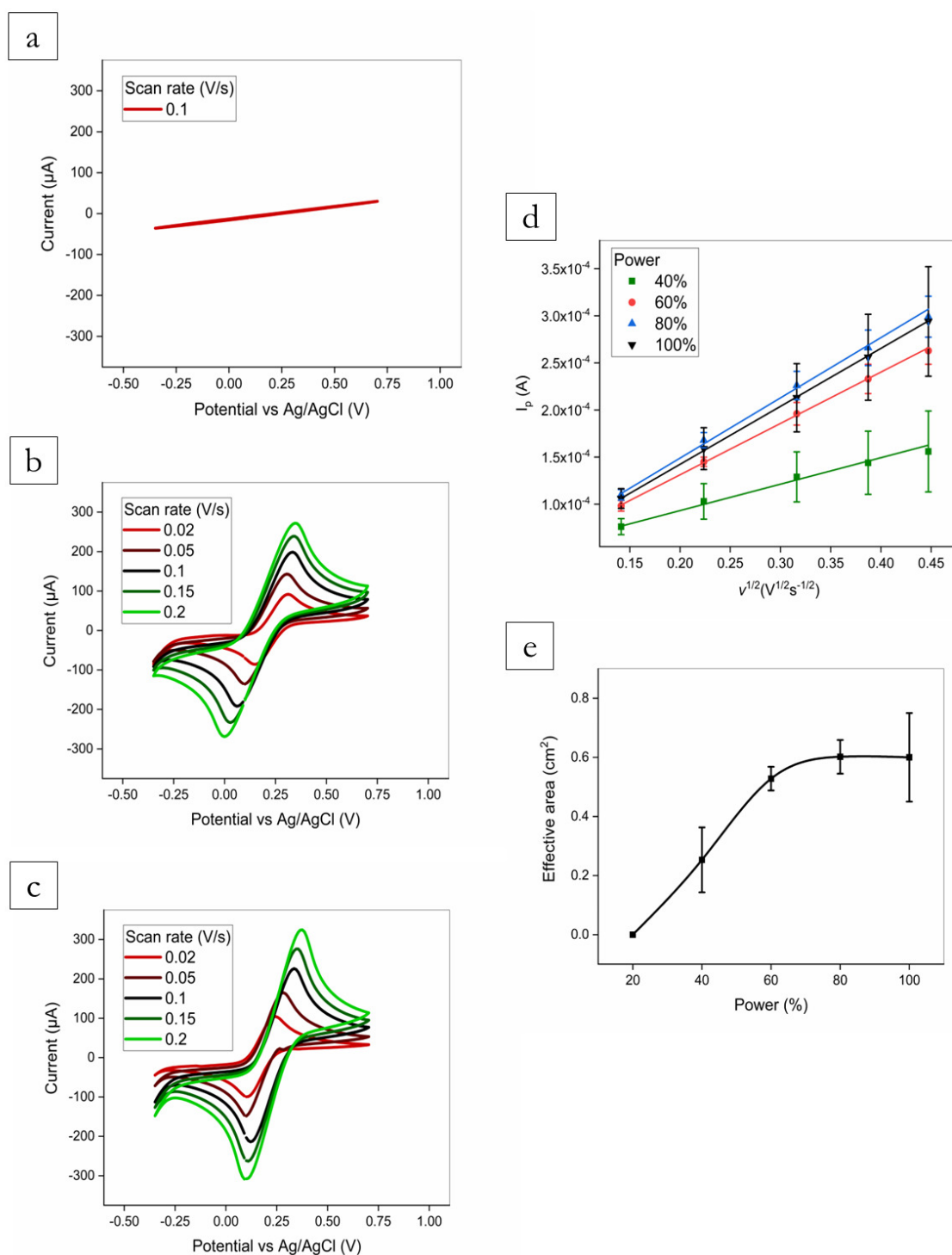


**Figure 4.** Cyclic voltammograms of (a) LIG20, (b) LIG60 and (c) LIG100. (d) Calibration curves graph. (e) Effective areas graph.

As for electrode sensitivity, we selected a scan rate of 0.1 V/s when comparing peak current values. LIG40 displayed the lowest peak currents and the highest difference between the potentials corresponding to these currents, suggesting a slow reaction rate likely attributed to electrode defects, such as conductivity failures due to non-uniform morphology (Supplemental Fig. 3) or mechanical instability. Peak current values also increased with increasing engraving power, with LIG80 demonstrating the highest average peak current, yielding a better sensitivity. Although LIG100 exhibited favorable average characteristics, it displayed significant variability in response from electrode to electrode, indicating irreproducibility that should be avoided in accurate sensing applications, as this would likely yield inconsistent results for this measurement.

As experimentally revealed that peak currents increase linearly with the square root of the scan rate (Fig. 4d), we modeled the reaction using the Randles-Sevcik equation [41] for the ferri/ferrocyanide reaction. In this case,  $T = 25$  °C (temperature),  $n = 1$  (number of electrons transferred),  $D = 6.36 \times 10^{-6}$  (diffusion coefficient of the electroactive species), and  $C = 2.5$  mol/cm<sup>3</sup> (concentration of the species in solution). Observing this linear behavior between  $I_p$  and  $v^{1/2}$ , we can assert that the slopes represent the ratio between these variables, which allows for determining the effective area for the four working electrodes (Fig. 4e). Considering that the theoretical geometric contact area of the electrodes is  $\sim 0.358$  cm<sup>2</sup>, we drew the following observations: WE of LIG20 exhibited no electrochemical response, which indicates zero involvement of area in the reaction, resulting in an electrochemically active surface area (EASA) [42] of 0. LIG40 displayed an average EASA of approximately  $\sim 0.253$  cm<sup>2</sup>, indicating an electrochemical roughness (EASA/geometric active area ratio) below 1, which implies that, at low power, the electrode area does not interact with the ferri-ferrocyanide solution. LIG60 and LIG80 deviated minimally from one another and exhibited identical characteristics, indicating reproducibility. Moreover, the effective area was approximately 50 %–70 % larger than the geometric area, aligning with Soares *et al.* [43] and Nayak *et al.* [44] findings. This augmented area is attributed to the transformation to LIG at these power levels, owing to its porosity, suggesting an increased space for the reaction, facilitated by the exposure of more edge planes of graphene to the redox solution, enhancing electron transfer and, consequently, elevating the EASA [43]. LIG100's WE exhibited a significantly high deviation, showing an effective area even twice the geometric contact area, while others presented only half; morphological damages (Fig. 2c) can contribute to this lack of consistency, rendering this power set unreliable for electrochemical analysis. Therefore, these settings should be avoided when developing future sensors, as they would likely yield inconsistent sensing results for this measurement.

Building upon previous characterizations' findings, we can choose the most favorable parameters based on electrode physical and electrochemical performances. Eliminating low speeds is motivated by the imperative of time optimization, and low and high powers were ruled out due to elevated resistivities following electrical measurements. At low power, polyimide was insufficiently transformed by LIG, resulting in a high defect rate, poor current ratio, and low sensitivity, as revealed by our morphological, structural, and electrochemical characterizations, respectively. At high power, the characteristics, except morphology, show improvement; however, the error percentages are much higher, significantly reducing their repeatability, thus restricting the selection to the 60 % and 80 % power range with a 91 % speed for a satisfactory subsequent fabrication of efficient sensors.

## 4. Conclusions

Varying LIG fabrication parameters enabled the tuning of physical and electrochemical properties in LIG-based electrodes. By altering the laser's power and speed settings, we observed a significant sensitivity of these variables on the physicochemical properties of the electrodes. Achieving a correct balance between power and speed is crucial for controlling the energy density applied to the substrate, which, in turn, governs the carbonization degree. Our custom-built structure, equipped with a 5W UV-VIS diode laser, demonstrated the capacity to achieve polyimide-to-LIG transformation, producing microstructures and sheet resistances comparable to those reported for UV and CO<sub>2</sub> lasers.

Electrochemical results were consistent with physical characterization: electrodes exhibiting early-stage porous formations had limited conductivity, which hindered the development of an electrochemically active area. In contrast, regions with well-formed cell networks and fibers (as observed in SEM images) showed improved electrochemical performance due to the increased porosity, which enhanced the reaction area. Microstructural and electrochemical characteristics improved at higher powers, such as larger effective areas and more pronounced porous formations. However, at higher power settings, variability in electrode performance emerged. Despite exhibiting conductivity and electrochemical responses, the electrodes subjected to high power revealed morphological damage, which reduced their mechanical integrity and introduced inconsistencies in their assessments. This variability also influenced their sheet resistance data and microstructural characterizations (Raman), leading to electrochemical performance, structural quality, and sheet resistance fluctuations. The power range between 60 % and 80 % at a 91 % speed rate exhibited minimal variation in sensor performance, reflecting a consistent and reliable outcome across different samples. This range ensures a balance of conductivity, sensitivity, and reproducibility, making it ideal for reliable sensor fabrication.

This study highlights the potential of using a custom-built CNC system with a laser to fabricate high-performance LIG electrodes. Our analysis enhances the understanding of LIG morphologies and properties and contributes to the broader discussion on LIG applications in detecting analytes critical to human health.

## 5. Acknowledgements

This work was partially funded by the Colombian Ministry of Science, Technology, and Innovation MINCIENCIAS (under call 932 of 2022). Authors also thank to Laboratorio de Física del Plasma at Universidad Nacional de Colombia sede Manizales, and Tecnoparque SENA, nodo Cali for their technical support.

## 6. Conflict of interest

The authors declare that they have no affiliations with or involvement in any organization or entity with any financial interest (such as honoraria; educational grants; participation in speakers' membership, employment, consultancies, stock ownership, or other equity interest; and expert testimony or patent arrangements), or non (such as personal or professional relationships, affiliations, knowledge or beliefs) in the subject matter or materials discussed in this manuscript.

## References

- [1] Tiwari SK, Sahoo S, Wang N, Huczko A, Graphene research and their outputs: Status and prospect, *Journal of Science: Advanced Materials and Devices*, 5:10–29, 2020.  
<https://doi.org/10.1016/j.jsamd.2020.01.006>.
- [2] Madurani KA, Suprpto S, Machrita NI, Bahar SL, Illiya W, Kurniawan F, Progress in Graphene Synthesis and its Application: History, Challenge and the Future Outlook for Research and Industry, *ECS Journal of Solid State Science and Technology*. 9: 093013, 2020.  
<https://doi.org/10.1149/2162-8777/abbb6f>.
- [3] Wu S, He Q, Tan C, Wang Y, Zhang H, Graphene-Based Electrochemical Sensors, *Small*, 9: 1160–1172, 2013.  
<https://doi.org/10.1002/sml.201202896>.
- [4] Fahmy Taha M, Ashraf H, Caesarendra W, A Brief Description of Cyclic Voltammetry Transducer-Based Non-Enzymatic Glucose Biosensor Using Synthesized Graphene Electrodes, *ASI* 3:32, 2020.  
<https://doi.org/10.3390/asi3030032>.
- [5] Zhen Z, Zhu H, Structure and properties of graphene, in: *Graphene: Fabrication, Characterizations, Properties and Applications*, pp. 1–12, 2018.  
<https://doi.org/10.1016/B978-0-12-812651-6.00001-X>.
- [6] Yang G, Li L, Lee WB, Ng MC, Structure of graphene and its disorders: a review, *Science and Technology of Advanced Materials* 19: 613–648, 2018.  
<https://doi.org/10.1080/14686996.2018.1494493>.
- [7] Olabi AG, Abdelkareem MA, Wilberforce T, Sayed ET, Application of graphene in energy storage device - A review, *Renewable and Sustainable Energy Reviews* 135: 110026, 2021.  
<https://doi.org/10.1016/j.rser.2020.110026>.
- [8] Lahcen AA, Rauf S, Beduk T, Durmus C, Aljedaibi A, Timur S, Alshareef HN, Amine A, O.S. Wolfbeis, K.N. Salama, Electrochemical sensors and biosensors using laser-derived graphene: A comprehensive review, *Biosensors and Bioelectronics*, 168: 112565, 2020.  
<https://doi.org/10.1016/j.bios.2020.112565>.
- [9] Wang F, Wang K, Zheng B, Dong X, Mei X, Lv J, Duan W, Wang W, Laser-induced graphene: preparation, functionalization and applications, *Materials Technology*, 33: 340–356, 2018.  
<https://doi.org/10.1080/10667857.2018.1447265>.
- [10] Kaidarova A, Kosel J, Physical Sensors Based on Laser-Induced Graphene: A Review, *IEEE Sensors J.* 21: 12426–12443, 2021.  
<https://doi.org/10.1109/JSEN.2020.3034845>.

- [11] Le TD, Phan H, Kwon S, Park S, Jung Y, Min J, Chun BJ, Yoon H, Ko SH, Kim S, Kim Y, Recent Advances in Laser-Induced Graphene: Mechanism, Fabrication, Properties, and Applications in Flexible Electronics, *Advanced Functional Materials* 32: 2205158, 2022.  
<https://doi.org/10.1002/adfm.202205158>.
- [12] Liu J, Bao S, Wang X. Applications of Graphene-Based Materials in Sensors: A Review, *Micromachines* 13: 184, 2022.  
<https://doi.org/10.3390/mi13020184>.
- [13] Wu Y, Zhu J, Huang L, A review of three-dimensional graphene-based materials: Synthesis and applications to energy conversion/storage and environment, *Carbon* 143: 610-640, 2019.  
<https://doi.org/10.1016/j.carbon.2018.11.053>.
- [14] Lin J, Peng Z, Liu Y, Ruiz-Zepeda F, Ye R, Samuel ELG, Yacaman MJ, Yakobson BI, Tour JM, Laser-induced porous graphene films from commercial polymers, *Nature Communications* 5: 15-18, 2014.  
<https://doi.org/10.1038/ncomms6714>.
- [15] Shams SS, Zhang R, Zhu J, Graphene synthesis: a Review, *Materials Science-Poland* 33: 566-578, 2015.  
<https://doi.org/10.1515/msp-2015-0079>.
- [16] Santhiran A, Iyngaran P, Abiman P, Kuganathan N, Graphene Synthesis and Its Recent Advances in Applications-A Review, *Journal of Carbon Research*, 7(4): 76, 2021.  
<https://doi.org/10.3390/c7040076>.
- [17] Agudosi ES, Abdullah EC, Numan A, Mubarak NM, Khalid M, Omar N, A Review of the Graphene Synthesis Routes and its Applications in Electrochemical Energy Storage, *Critical Reviews in Solid State and Materials Sciences* 45: 339-377, 2020.  
<https://doi.org/10.1080/10408436.2019.1632793>.
- [18] Lee XJ, Hiew BYZ, Lai KC, Lee LY, Gan S, Thangalazhy-Gopakumar S, Rigby S, Review on graphene and its derivatives: Synthesis methods and potential industrial implementation, *Journal of the Taiwan Institute of Chemical Engineers* 98:163-180, 2019.  
<https://doi.org/10.1016/j.jtice.2018.10.028>.
- [19] Nag A, Mitra A, Mukhopadhyay SC, Graphene and its sensor-based applications: A review, *Sensors and Actuators A: Physical* 270: 177-194, 2018.  
<https://doi.org/10.1016/j.sna.2017.12.028>.
- [20] Zhang J, Xu R, Feng J, Xie Y, Zhou T, Laser Direct Writing of Flexible Heaters on Polymer Substrates, *Industrial & Engineering Chemistry Research*. 60: 11161-11170, 2021.  
<https://doi.org/10.1021/acs.iecr.1c02358>.

- [21] Xu Y, Fei Q, Page M, Zhao G, Ling Y, Chen D, Yan Z, Laser-induced graphene for bioelectronics and soft actuators, *Nano Research*, 14: 3033-3050, 2021.  
<https://doi.org/10.1007/s12274-021-3441-9>.
- [22] Wan Z, Umer M, Lobino M, Thiel D, Nguyen NT, Trinchi A, Shiddiky MJA, Gao Y, Li Q, Laser induced self-N-doped porous graphene as an electrochemical biosensor for femtomolar miRNA detection, *Carbon*, 163: 385-394, 2020.  
<https://doi.org/10.1016/j.carbon.2020.03.043>.
- [23] Abdulhafez M, Tomaraei GN, Bedewy M, Fluence-Dependent Morphological Transitions in Laser-Induced Graphene Electrodes on Polyimide Substrates for Flexible Devices, *ACS Applied Nano Materials*, 4: 2973-2986, 2021.  
<https://doi.org/10.1021/acsanm.1c00101>.
- [24] Duy LX, Peng Z, Li Y, Zhang J, Ji Y, Tour JM, Laser-induced graphene fibers, *Carbon*, 126: 472-479, 2018.  
<https://doi.org/10.1016/j.carbon.2017.10.036>.
- [25] Laserax, Láser de co2 frente a láser de fibra: ¿cuál debería de comprar? Laserax, 2020.  
<https://www.laserax.com/es/blog/laser-co2-frente-laser-fibra-cual-deberia-comprar>.
- [26] Liu X, Zhang F, Zhang Q, Wan Z, Chen X, Laser-scribed graphene for sensors: preparation, modification, applications, and future prospects, *Light: Advanced Manufacturing* 4(2): 143-167, 2023.  
<https://doi.org/10.37188/lam.2023.011>.
- [27] Suvarnaphaet P, Pechprasarn S, Graphene-Based Materials for Biosensors: A Review, *Sensors*, 17(10): 2161, 2017.  
<https://doi.org/10.3390/s17102161>.
- [28] Balkourani G, Damartzis T, Brouzgou A, Tsiakaras P, Cost Effective Synthesis of Graphene Nanomaterials for Non-Enzymatic Electrochemical Sensors for Glucose: A Comprehensive Review, *Sensors*, 22(1): 355, 2022.  
<https://doi.org/10.3390/s22010355>.
- [29] Le TD, Park S, An J, Lee PS, Kim Y, Ultrafast Laser Pulses Enable One-Step Graphene Patterning on Woods and Leaves for Green Electronics, *Advanced Functional Materials*, 29: 1902771, 2019.  
<https://doi.org/10.1002/adfm.201902771>.
- [30] Zhu Y, Cai H, Ding H, Pan N, Wang X, Fabrication of Low-Cost and Highly Sensitive Graphene-Based Pressure Sensors by Direct Laser Scribing Polydimethylsiloxane, *ACS Applied Materials & Interfaces* 11(6): 6195-6200, 2019.  
<https://doi.org/10.1021/acsam.8b17085>.

- [31] Zhang Z, Song M, Hao J, Wu K, Li C, Hu C, Visible light laser-induced graphene from phenolic resin: A new approach for directly writing graphene-based electrochemical devices on various substrates, *Carbon* 127: 287-296, 2018.  
<https://doi.org/10.1016/j.carbon.2017.11.014>.
- [32] Stanford MG, Zhang C, Fowlkes JD, Hoffman A, Ivanov IN, Rack PD, Tour JM, High-Resolution Laser-Induced Graphene. Flexible Electronics beyond the Visible Limit, *ACS Applied Materials & Interfaces* 12: 10902-10907, 2020.  
<https://doi.org/10.1021/acsami.0c01377>.
- [33] Lei Y, Alshareef AH, Zhao W, Inal S, Laser-Scribed Graphene Electrodes Derived from Lignin for Biochemical Sensing, *ACS Applied Nano Materials*, 3: 1166-1174, 2020.  
<https://doi.org/10.1021/acsanm.9b01795>.
- [34] Zhang W, Lei Y, Ming F, Jiang Q, Costa PMFJ, Alshareef HN, Lignin Laser Lithography: A Direct-Write Method for Fabricating 3D Graphene Electrodes for Microsupercapacitors, *Advanced Energy Materials*, 8: 1801840, 2018.  
<https://doi.org/10.1002/aenm.201801840>.
- [35] de la Roche J, López-Cifuentes I, Jaramillo-Botero A, Influence of lasing parameters on the morphology and electrical resistance of polyimide-based laser-induced graphene (LIG), *Carbon Letters*, 33: 587-595, 2022.  
<https://doi.org/10.1007/s42823-022-00447-2>.
- [36] Luong DX, Yang K, Yoon J, Singh SP, Wang T, Arnusch CJ, Tour JM, Laser-Induced Graphene Composites as Multifunctional Surfaces, *ACS Nano*, acsnano.8b09626, 2019.  
<https://doi.org/10.1021/acsnano.8b09626>.
- [37] Edberg J, Brooke R, Hosseinaei O, Fall A, Wijeratne K, Sandberg M, Laser-induced graphitization of a forest-based ink for use in flexible and printed electronics, *Flexible Electronics*, 4: 17, 2020.  
<https://doi.org/10.1038/s41528-020-0080-2>.
- [38] Ferrari AC, Meyer JC, Scardaci V, Casiraghi C, Lazzeri M, Mauri F, Piscanec S, Jiang D, Novoselov KS, Roth S, Geim AK, Raman Spectrum of Graphene and Graphene Layers, *Physical Review Letters*, 97: 187401, 2006.  
<https://doi.org/10.1103/PhysRevLett.97.187401>.
- [39] Carvalho AF, Fernandes AJC, Leitão C, Deuermeier J, Marques AC, Martins R, Fortunato E, Costa FM, Laser-Induced Graphene Strain Sensors Produced by Ultraviolet Irradiation of Polyimide, *Advanced Functional Materials* 28: 1805271, 2018.  
<https://doi.org/10.1002/adfm.201805271>.

- [40] Herziger F, Mirzayev R, Poliani E, Maultzsch J, In-situ Raman study of laser-induced graphene oxidation: In-situ Raman study of laser-induced graphene oxidation, *Physical Status Solidi B*, 252: 2451-2455, 2015.  
<https://doi.org/10.1002/pssb.201552411>.
- [41] Krejci J, Sajdlova Z, Nedela V, Flodrova E, Sejnohova E, Vranova H, Plicka R, Effective Surface Area of Electrochemical Sensors, *Journal of the Electrochemical Society*, 161: B147-B150, 2014.  
<https://doi.org/10.1149/2.091406jes>.
- [42] Muzyka K, Xu G, Laser-Induced Graphene in Facts, Numbers, and Notes in View of Electroanalytical Applications: A Review, *Electroanalysis*, 34: 574-589, 2022.  
<https://doi.org/10.1002/elan.202100425>.
- [43] Soares RRA, Hjort RG, Pola CC, Parate K, Reis EL, Soares NFF, McLamore ES, Claussen JC, Gomes CL, Laser-Induced Graphene Electrochemical Immunosensors for Rapid and Label-Free Monitoring of Salmonella enterica in Chicken Broth, *ACS Sensors*, 5: 1900-1911, 2020.  
<https://doi.org/10.1021/acssensors.9b02345>.
- [44] Nayak P, Kurra N, Xia C, Alshareef HN, Highly Efficient Laser Scribed Graphene Electrodes for On-Chip Electrochemical Sensing Applications, *Advanced Electronic Materials*, 2: 1600185, 2016.  
<https://doi.org/10.1002/aelm.201600185>.

### Efectos de los parámetros láser UV-VIS en las propiedades fisicoquímicas del grafeno inducido por láser)

**Resumen:** El grafeno inducido por láser (LIG, por sus siglas en inglés) es una técnica versátil y escalable para la producción de dispositivos sensores de tipo grafeno a bajo costo. Sin embargo, el desempeño de estos dispositivos es altamente sensible a los parámetros de grabado utilizados durante su fabricación. En este trabajo, variamos sistemáticamente la velocidad y la potencia del grabado láser para explorar su influencia en las propiedades físicas y electroquímicas de los electrodos de LIG, con el objetivo de lograr una baja resistencia, alta porosidad del LIG y una sensibilidad mejorada para futuras aplicaciones en sensores. Empleamos un láser de diodo UV-VIS montado en un sistema CNC (Control Numérico por Computadora) construido por nuestro equipo, para grabar láminas de poliimida. Nuestros resultados demostraron que los ajustes de baja y alta potencia generaron un bajo desempeño de los electrodos debido al aumento de la resistividad y a los daños estructurales. En cambio, los electrodos fabricados con configuraciones de potencia entre el 60 % (3W) y el 80 % (4W) de la capacidad máxima del láser, combinadas con la velocidad operativa máxima, exhibieron una morfología uniforme, alta conductividad y un comportamiento electroquímico reversible. Bajo estas condiciones, los electrodos basados en LIG resultantes presentaron grafeno poroso en redes con asimetría direccional, con una relación  $I_D/I_G$  de aproximadamente 1,3, una resistencia por hoja de  $20 \Omega/\text{cuadrado}$  y una corriente pico de  $272,1 \mu\text{A}$ , junto con una relación  $I_{pa}/I_{pc}$  cercana a 1 en las mediciones de voltametría cíclica, proporcionando así una base sólida para el desarrollo de sensores eficientes basados en LIG.

**Palabras Clave:** Grafeno inducido por láser (LIG); Láser de diodo UV-VIS; Microestructura Parámetros de grabado; Propiedades electroquímicas.

### Efeitos dos parâmetros do laser UV-VIS nas propriedades físico-químicas do grafeno induzido por laser)

**Resumo:** O grafeno induzido por laser (LIG, na sigla em inglês) é uma técnica versátil e escalável para a produção de dispositivos sensores do tipo grafeno a baixo custo. No entanto, o desempenho desses dispositivos é altamente sensível aos parâmetros de gravação utilizados durante a sua fabricação. Neste trabalho, variamos sistematicamente a velocidade e a potência da gravação laser para explorar sua influência nas propriedades físicas e eletroquímicas dos eletrodos de LIG, com o objetivo de alcançar baixa resistência, alta porosidade do LIG e sensibilidade aprimorada para futuras aplicações em sensores. Empregamos um laser de diodo UV-VIS montado em um sistema CNC (Controle Numérico Computadorizado) construído por nossa equipe, para gravar folhas de poliimida. Nossos resultados demonstraram que os ajustes de baixa e alta potência resultaram em baixo desempenho dos eletrodos devido ao aumento da resistividade e aos danos estruturais. Por outro lado, os eletrodos fabricados com configurações de potência entre 60 % (3W) e 80 % (4W) da capacidade máxima do laser, combinadas com a velocidade operacional máxima, apresentaram morfologia uniforme, alta condutividade e comportamento eletroquímico reversível. Sob essas condições, os eletrodos resultantes baseados em LIG apresentaram grafeno poroso em redes com assimetria direcional, com uma razão  $I_D/I_G$  de aproximadamente 1,3, uma resistência por folha de 20  $\Omega$ /quadrado e uma corrente de pico de 272,1  $\mu$ A, juntamente com uma razão  $I_{pa}/I_{pc}$  próxima de 1 nas medições de voltametria cíclica, fornecendo assim uma base sólida para o desenvolvimento de sensores eficientes baseados em LIG.

**Palavras-chave:** Bioinformática; derivados de quinina; metabólito secundário; predição de rotas; prospecção de fármacos antimaláricos.

**Jhonattan de la Roche**

He holds a Ph.D. in Materials Science and has international research experience in Mexico and Spain. His work focuses on materials processing, with applications in wear resistance, corrosion, and thermal protection. He has published in Q1 journals and has expertise in project formulation and management. Currently, he is the Scientific Director of CDT Innterfaz at Universidad Nacional de Colombia, providing consulting services in materials and processes.

ORCID: 0000-0003-3131-3096

**Carlos Lubo-Mestanza**

Physics Engineer from Universidad Nacional de Colombia, Manizales, and a Master's student in Physics at the same institution. He has expertise in the synthesis, characterization, and application of materials and biomaterials. Currently, he is researcher at Universidad Nacional de Colombia, Bogotá, specializing in nanomaterials and quantum technologies.

ORCID: 0009-0006-9176-0655

**Laura Tenjo-Patiño**

received a B.S. in Engineering Physics from Universidad Nacional de Colombia (2024) and is currently pursuing an M.Sc. in Physics, focusing on quantum computing. She has research experience in quantum technologies and materials science, including a research internship in particle physics in Spain.

ORCID: 0009-0006-3002-3918

**Santiago Lasso**

He is Physics Engineer with expertise in the synthesis, characterization, and application of materials and biomaterials.

ORCID: 0009-0005-2899-3643

**Santiago Ospina-Arroyave**

He is a physical engineer specialized in PVD coatings. His current work is production coordinator in tecnoglass sas.

ORCID: 0000-0001-8045-3381

**Sebastián Mendoza**

He is a physical engineer with a master's degree in physical sciences, specialized in PVD coatings. He has worked as a researcher and project manager, leading technological scaling. He has publications in indexed scientific journals, experience in electron microscopy and technology transfer.

ORCID: 0000-0001-9458-6556

**Lucero Álvarez Miño**

She is a physicist with a PhD from Universidad Nacional de Colombia and postgraduate studies at the Abdus Salam ICTP. Since 1996, she has been a professor at the National University of Colombia in Manizales, currently holding a tenured Associate Professorship. Her research focuses on condensed matter physics, particularly thin films, including metallic and superconducting films, and manganite-based devices. She is also involved in science education and communication research.

ORCID: 0000-0002-3046-7504